



# AMERICAN METEOROLOGICAL SOCIETY

*Monthly Weather Review*

## **EARLY ONLINE RELEASE**

This is a preliminary PDF of the author-produced manuscript that has been peer-reviewed and accepted for publication. Since it is being posted so soon after acceptance, it has not yet been copyedited, formatted, or processed by AMS Publications. This preliminary version of the manuscript may be downloaded, distributed, and cited, but please be aware that there will be visual differences and possibly some content differences between this version and the final published version.

The DOI for this manuscript is doi: 10.1175/MWR-D-17-0240.1

The final published version of this manuscript will replace the preliminary version at the above DOI once it is available.

If you would like to cite this EOR in a separate work, please use the following full citation:

Annane, B., B. McNoldy, S. Leidner, R. Hoffman, R. Atlas, and S. Majumdar, 2018: A Study of the HWRF Analysis and Forecast Impact of Realistically Simulated CYGNSS Observations Assimilated as Scalar Wind Speeds and as VAM Wind Vectors. *Mon. Wea. Rev.* doi:10.1175/MWR-D-17-0240.1, in press.



A Study of the HWRF Analysis and Forecast Impact of Realistically Simulated CYGNSS  
Observations Assimilated as Scalar Wind Speeds and as VAM Wind Vectors

*To be submitted to Monthly Weather Review.*

Bachir Annane\*

*NOAA Atlantic Oceanographic and Meteorological Laboratory, Miami FL and Cooperative  
Institute for Marine and Atmospheric Studies, University of Miami, Miami, FL*

Brian McNoldy

*Rosenstiel School of Marine and Atmospheric Science, University of Miami, Miami, FL*

S. Mark Leidner

*Atmospheric and Environmental Research, a Verisk Analytics company, Lexington, MA*

Ross Hoffman

*NOAA Atlantic Oceanographic and Meteorological Laboratory, Miami FL and Cooperative  
Institute for Marine and Atmospheric Studies, University of Miami, Miami, FL*

Robert Atlas

*NOAA/Atlantic Oceanographic and Meteorological Laboratory, Miami, Florida*

Sharanya J. Majumdar

*Rosenstiel School of Marine and Atmospheric Science, University of Miami, Miami, FL*

*\*Corresponding author address: Cooperative Institute for Marine and Atmospheric Studies  
(CMAS), Rosenstiel School of Marine and Atmospheric Science (RSMAS), University of Miami,  
4600 Rickenbacker Causeway, Key Biscayne, FL 33149 E-mail: [bachir.annane@noaa.gov](mailto:bachir.annane@noaa.gov)*

1 Abstract

2

3 In preparation for the launch of the NASA Cyclone Global Navigation Satellite System (CYGNSS),  
4 a variety of observing system simulation experiments (OSSEs) were conducted to develop, tune,  
5 and assess methods of assimilating these novel observations of ocean surface winds. From a  
6 highly detailed and realistic hurricane nature run (NR), CYGNSS winds were simulated with error  
7 characteristics that are expected to occur in reality. The OSSE system makes use of NOAA's  
8 HWRF model and GSI data assimilation system in a configuration that was operational in 2012.  
9 CYGNSS winds were assimilated as scalar wind speeds and as wind vectors determined by a  
10 Variational Analysis Method (VAM). Both forms of wind information had positive impacts on  
11 the short-term HWRF forecasts, as shown by key storm and domain metrics. Data assimilation  
12 cycle intervals of 1, 3, and 6 hours were tested, and the 3-h impacts were consistently best. One  
13 day forecasts from CYGNSS VAM vector winds were the most dynamically consistent with the  
14 NR. The OSSEs have a number of limitations- most noteworthy that this is a case study and  
15 static background error covariances were used.

16 1. Introduction

17 Ocean surface wind observations from satellites have been shown to improve the accuracy of  
18 numerical weather analyses and forecasts (Atlas 2001,1997; Candy et al. 2009; Leidner et al.  
19 2003; Shultz et al. 2007). Accurate surface wind analyses and forecasts are key to estimating  
20 the potential damage from storm surge (the deadliest tropical storm hazard; Rapport et al.,  
21 2009; Powell and Reinhold, 2007) and wind. However, most current satellite observing systems  
22 are unable to provide accurate ocean surface wind speed data in areas of precipitation and  
23 generally have limited temporal resolution (e.g., 1-2 overpasses/day). Of all these systems, only  
24 L-band sensors such as those on the Soil Moisture Active Passive (SMAP, Entekhabi et al. 2010 )  
25 satellite and the NASA Cyclone Global Navigation Satellite System (CYGNSS, Ruf et al. 2016a)  
26 can observe winds in the presence of heavy rain, such as occurs in the inner core of a tropical  
27 cyclone (TC). CYGNSS is expected to alleviate some of the current deficiencies in temporal and  
28 spatial sampling of the surface wind field of tropical cyclones. CYGNSS is also expected to  
29 provide improved wind speed observing capabilities to observe the structure and evolution of  
30 TCs. This will also improve the accuracy of the wind products that are inputs to storm surge  
31 models, e.g., the Coastal and Estuarine Storm Tide (CEST) and the Sea, Lake, and Overland  
32 Surge from Hurricane (SLOSH).

33 This study focuses on the impact of accurate near-surface wind observations over the ocean on  
34 numerical weather prediction (NWP) analyses and forecasts directly. It should be noted that  
35 such data also have the potential to indirectly improve NWP by improving the model  
36 parameterizations of wind stress and sensible and latent heat fluxes. These processes are

37 critical to air-sea interactions parameterized in global and regional weather forecast models  
38 and are key to our understanding of the atmosphere-ocean system. Through assimilation of  
39 such wind data, the depiction of the boundary layer can also be improved in weather forecast  
40 models (Atlas et al. 1999, 2001, 2015).

41 Improvements in tropical cyclone forecasts over the past few decades have mainly been due to  
42 advances in numerical models (Atlas et al.2015; Gopalakrishnan et al. 2012; Rappaport et al.  
43 2009; Willoughby, 2009). However, forecasting the intensity change of tropical cyclones  
44 remains a challenging problem. One reason for the slower improvement in intensity forecasts  
45 compared to track forecasts is the lack of frequent sampling of the inner core of the storm  
46 (Rogers et al. 2013). Presently, only TC-penetrating aircraft collect measurements in the inner  
47 core. These *in situ* measurements are only collected for about 30% of the lifetimes of tropical  
48 cyclones in the Atlantic and even less in the eastern North Pacific (Rappaport et al., 2009).  
49 Reconnaissance aircraft (Aberson et al. 2006) such as the NOAA P-3 host the most advanced  
50 and accurate instrumentation, including stepped frequency microwave radiometers (SFMR,  
51 Uhlhorn et al., 2007) and Global Positioning System (GPS) dropwindsondes (Hock and Franklin,  
52 1999). With limited dwell time and limited resources (aircraft, dropsondes), the inner cores of  
53 even the best-monitored TCs are relative data voids (Uhlhorn and Nolan 2012). A single well-  
54 placed dropwindsonde, properly reduced by empirical methods to 10-m equivalent wind speed,  
55 can estimate maximum surface wind speed and hence the TC intensity. However, a fleet of  
56 dropwindsondes would be required to map out the complete TC surface wind field to depict the  
57 full destructive potential of a storm (Powell and Reinhold, 2007).

58 CYGNSS was designed to address these observational deficiencies. The CYGNSS GPS receivers  
59 hosted on eight minisats were launched 17 December 2016 measure reflected ocean surface  
60 signals of opportunity (SoO) broadcast by the existing GPS satellites. This bistatic configuration,  
61 in which the transmitter and receiver are on different platforms (Fig. 1), contrasts with the  
62 monostatic configuration of scatterometers in which the transmitter and receiver are  
63 colocated. Using a constellation of eight small satellites at an altitude of 510 km in a single, low-  
64 inclination ( $35^\circ$ ) orbit plane, CYGNSS samples the tropics and subtropics at a nominal spatial  
65 resolution of 25 km with improved temporal sampling compared to polar orbiting satellites. For  
66 any given area on earth between  $38^\circ$  north and south latitude, the spatial and temporal  
67 sampling of the ocean surface by CYGNSS constellation is random, since the movements of the  
68 GPS and CYGNSS constellations are not coordinated (Ruf, et al, 2016b). But the orbits of the  
69 CYGNSS constellation generally produce measured reflections over an area the size of a typical  
70 tropical cyclone for two, 90-minute periods each day, separated by about 12 hours. An  
71 example of simulated, 6-hour coverage over the North Atlantic is shown and described below  
72 (Section 2.2.2).

73 The goal of the study presented here is to assess the potential utility of CYGNSS observations of  
74 ocean surface wind for hurricane analysis and forecasting. How might CYGNSS data be  
75 expected to improve or change the analysis and forecasts of tropical cyclones when  
76 incorporated into a hurricane analysis and forecast system? What methods work best to  
77 extract information from the CYGNSS observations? These questions are examined with an  
78 observing system simulation experiment (OSSE) approach (Hoffman and Atlas, 2016). The  
79 experiments conducted extend the experiments of McNoldy et al. (2017, hereafter M17). Both

80 M17 and the present study conducted OSSEs using the NOAA's Atlantic Oceanographic and  
81 Meteorological Laboratory (AOML) hurricane OSSE system that assimilates CYGNSS  
82 observations simulated in different ways during the lifetime of one simulated hurricane. In an  
83 OSSE, the Nature Run (NR), or truth, provides both a point of comparison for OSSE experiment  
84 results, as well as the source for simulating all observations assimilated. In this study, a pair of  
85 self-consistent global and regional NRs are used: the ECMWF model (T511 NR) and an  
86 embedded Advanced Research Weather Research and Forecasting (WRF-ARW) nested high-  
87 resolution (up to 1-km resolution) simulation.

88 M17 found a positive impact on TC analyses and forecasts of adding CYGNSS observations to a  
89 control experiment through a progression of four experiments which added (1) realistic CYGNSS  
90 wind speed observations retrieved at high (12.5-km) resolution, (2) at nominal (25-km)  
91 resolution, (3) perfect wind speed observations, and (4) perfect wind vector observations. Both  
92 perfect simulated CYGNSS observation datasets (3, 4) are at the same resolution (12.5-km) and  
93 spatial coverage. The noisy high-resolution winds had the smallest impact because the QC  
94 procedures rejected much of these data. For this reason, experiments in this study use only  
95 nominal-resolution CYGNSS winds. The control experiment and experiment 2 of M17 form the  
96 baseline for the new experiments described here and are denoted CTRL6 and CYG6 below. The  
97 25-km resolution simulated CYGNSS wind speeds of M17 are the basis of all experiments  
98 reported here.

99 Furthermore, in the present study, motivated by the very good results of experiment 4 of M17,  
100 direct assimilation of the CYGNSS wind speeds is compared to the assimilation of CYGNSS VAM

101 wind vectors created from the wind speeds as described by Leidner et al. (2017, hereafter L17).  
102 As described in detail by L17, the CYGNSS VAM wind vectors are a result of a variational analysis  
103 that combines the CYGNSS wind speeds and a background wind field. In the present case, the  
104 background wind fields are 6-h forecasts of the surface wind from an HWRF control experiment  
105 described below in Section 3. While M17 considered perfect wind vectors, here the effect of  
106 observation errors is propagated from the CYGNSS raw observation to CYGNSS winds through  
107 the VAM.

108 In addition, since TCs evolve and propagate quickly, shorter DA cycle intervals might yield  
109 superior results. In the DA system used here, even though observation innovations are  
110 evaluated with respect to the background at the time of the observation, these innovations are  
111 all combined to influence the model state at the central analysis time. This approximation is  
112 most appropriate for short DA cycles. However, every time the model is initialized with  
113 observations, there is some adjustment. For TCs, this adjustment can result in substantial  
114 increases (spin-up) or decreases (spin-down) of intensity. Therefore, there are tradeoffs in  
115 selecting the optimal DA cycle interval. In this study, DA cycle intervals of 1, 3, and 6 hours are  
116 tested, whereas M17 used 6-h cycles in all experiments.

117 The paper is organized as follows. Section 2 describes the OSSE framework. Section 3 presents  
118 the experimental design and Section 4 the results. Section 5 summarizes the present study with  
119 a focus on its findings and its limitations and briefly describes future planned studies.

120

121 2. OSSE framework

122 To conduct realistic OSSEs related to hurricane analyses and forecasts, AOML and the University  
123 of Miami developed a new regional OSSE framework (Atlas et al. 2015 a, b,c, McNoldy et al.  
124 2017). A schematic of this OSSE framework is illustrated in Fig. 2.

125

## 126 2.1 Nature run

127 The OSSE framework is based on a high-resolution regional nature run (Nolan et al. 2013), called  
128 HNR1, that was created by embedding the Advanced Research Weather Research and  
129 Forecasting (WRF-ARW) model version 3.2.1 within a lower-resolution global nature run. HNR1  
130 has an outer fixed domain of 27-km grid spacing spanning the tropical Atlantic basin, and three  
131 telescoping storm-following nested domains of 9-, 3- and 1-km grid spacing. Sixty model layers  
132 span the vertical domain from the surface to 50 hPa. The boundary conditions are provided by a  
133 global nature run produced by the European Centre for Medium-range Weather Forecasts  
134 (ECMWF) (version c31r1) T511 model with 91 vertical levels, here called the T511 NR (Andersson  
135 and Masutani 2010). The T511 NR is a free-running forecast from 1200 UTC 1 May 2005 to 1200  
136 UTC 1 June 2006. The period of HNR1 is from 0000 UTC 29 July 2005 to 0000 UTC 11 August 2005.  
137 The two nature runs have similar storm tracks but in the regional nature run the hurricane is  
138 simulated with more realistic intensity, scale, and structure and undergoes rapid intensification  
139 during the period centered on 4 August 2005.

140

## 141 2.2. Simulated observations

142 Within a typical OSSE framework, all observations should be simulated from a relevant Nature  
143 Run and observation errors appropriate to each observation type should be added. In the

144 hurricane OSSE system, observations are simulated by sampling the observed quantities from  
145 the T511 NR for conventional and routinely assimilated satellite data, whereas the CYGNSS  
146 observations are simulated with CYGNSS Science Team End-to-end Simulator (E2ES; O'Brien  
147 2014) based on the HNR1 winds. Typical errors are added to the simulated conventional and  
148 satellite observations, while a wind retrieval error model assigns realistic errors to the  
149 simulated CYGNSS wind speed. In addition, vector winds are determined from simulated  
150 CYGNSS wind speeds using a 2D variational analysis method (VAM). The VAM analyzes the  
151 simulated CYGNSS wind speeds given an *a priori*, gridded ocean surface wind field. The resulting  
152 wind direction and speed in the VAM analysis are assigned at each CYGNSS retrieved wind  
153 location to produce VAM CYGNSS wind vectors. More detailed descriptions of the methods and  
154 data sources used to simulate observations in our study are provided below.

155

### 156 2.2.1 Conventional and satellite observations

157 Conventional and satellite observations corresponding to those assimilated in NCEP operations  
158 were simulated from the T511 NR described in section 2.1. Realistic observation errors by  
159 observation type are based on estimates in NCEP's Gridpoint Statistical Interpolation (GSI) and  
160 added to each simulated observation. The errors are drawn from a zero-mean Gaussian  
161 distribution using the O-B error estimates as the standard deviation (Errico et al., 2013).  
162 Because of the close correspondence between the global T511 NR and the embedded regional  
163 WRF-ARW HNR1, the simulated conventional and satellite observations reflect the same  
164 synoptic conditions as HNR1 used to simulate the CYGNSS observations, just realized by a global  
165 model. All conventional observations of temperature, winds, moisture, and surface pressure,

166 atmospheric motion vectors, and satellite data types that were in operational use in 2012 are  
167 simulated from the T511 NR. (See Table 1 of Atlas et al. 2015c for the detailed list of satellite  
168 data sources.)

169

### 170 2.2.2 CYGNSS wind speed observations

171 The NASA CYGNSS Science Team simulated the CYGNSS wind speed observations with the E2ES,  
172 which takes orbital ephemeris for the actual GPS and simulated CYGNSS satellites to simulate  
173 reflected power from the gridded ocean surface wind fields. The reflected GPS signal power  
174 from the central reflecting point, i.e., the specular point (SP, in Fig. 1), as well as weaker  
175 reflections from a region approximately 100 km around the SP known as the “glistening zone”,  
176 are recorded in the measurement space of GPS signal delay and Doppler shift, known as a  
177 delay-Doppler map (DDM). DDMs of reflected power (Watts) are converted to DDMs of bistatic  
178 radar cross section  $\sigma^0$  ( $m^2$ ). The  $\sigma^0$  DDMs are the primary input to the CYGNSS wind speed  
179 retrieval algorithm.

180

181 For HNR1, E2ES generated specular points at a cadence of 1 Hz, using the highest available  
182 resolution HNR1 grid (27, 9, 3 or 1 km). Fig. 3 shows simulated CYGNSS winds in the 27-km  
183 domain at 1500 UTC 3 August 2005. Since the outer three grids are available every 30 minutes  
184 and the innermost domain every 6 minutes, the maximum time difference between NR output  
185 is 15 minutes. As the HNR1 nested grids are storm-following, CYGNSS SPs in or near the inner  
186 core are simulated using 1-km resolution HNR1 winds. Specular points further from the  
187 hurricane are simulated using HNR1 grids at lower resolutions, depending on location.

188 Consequently, the highest resolution is utilized in the region of highest wind speeds. Note how  
189 the coverage changes as the observation window is shortened from +/- 3 hours, to +/- 1.5 hours  
190 to +/- 0.5 hours, corresponding time windows used for 6-hourly, 3-hourly and hourly data  
191 assimilation cycling. This change in sampling has important consequences for the impact of the  
192 assimilated data (explored further in Section 4).

193

194 The HNR1 winds sampled by the E2ES at the CYGNSS locations are “perfect”. E2ES simulates  
195 realistic variation in measurement uncertainties with two additive error components due to  
196 uncertainty in: (1) the calibration of  $\sigma^{\rho}$  DDMs and (2) the wind retrieval algorithm assuming  
197 perfectly calibrated  $\sigma^{\rho}$  DDMs. The  $\sigma^{\rho}$  DDM uncertainty term was determined by the CYGNSS  
198 Science Team from a Level 1 processing flowdown error budget to have zero mean and a  
199 standard deviation of  $1.2 \text{ m s}^{-1}$ . The wind retrieval error term is more complex, depending on  
200 wind speed and range-corrected gain (RCG). In a simulated calibration exercise, the mean and  
201 variance of non-normal Gaussian distributions (“generalized normal”) were fit to Level 2 data in  
202 four wind speed ranges and six RCG ranges. Using the wind speed from the HNR1 at the  
203 specular point and the RCG calculated from the orbital ephemeris, Gaussian pseudo-random  
204 errors are added to the perfect observations (O’Brien, pers. comm.). Observation error  
205 computed for the simulated CYGNSS retrieved winds is a mixture of two Gaussian errors, one  
206 normal and another non-normal with typical values of  $2\text{-}4 \text{ m s}^{-1}$ , depending on the factors  
207 described above.

208

209 2.2.3 VAM CYGNSS wind vector observations

210 CYGNSS data do not include wind direction. With alternative GPS receiver hardware or ground  
211 processing, direction might be extracted from the reflected signal (e.g., Komjathy et al., 2004).  
212 To assess the benefit of adding directional information, a 2-dimensional variational analysis  
213 method (VAM; Hoffman, 1982, 1984) is applied following L17 to simulated CYGNSS wind speeds  
214 to generate dynamically realistic vector wind field analyses. The VAM has been applied to  
215 determine wind direction from among 2-4 wind ambiguities from both NSCAT and QuikSCAT  
216 scatterometer missions (Hoffman et al., 2003). The VAM has also been used to generate nearly  
217 30 years of 6-hourly global ocean surface wind analyses, combining all available passive  
218 microwave and scatterometer data since 1987 (Atlas et al., 1996, 2011). The VAM uses an *a*  
219 *priori*, or first guess, gridded surface wind field as a starting point for each analysis. In this  
220 study, 6-h forecasts on a 9-km-resolution outer domain from an HWRF regional Control OSSE  
221 experiment (CTRL6, described below in Section 3) are used as the VAM analysis first guess  
222 fields. This choice of first guess winds is intended to emulate what might be the best available  
223 choice in real-time, operational forecasting. A VAM analysis is generated four times a day at  
224 0000, 0600, 1200 and 1800 UTC for the period of the OSSE (a 4-day period described below in  
225 Section 3). The VAM analysis u- and v-wind components are interpolated in space and time to  
226 the set of simulated CYGNSS wind speed locations assimilated. These derived observations are  
227 referred to hereafter as VAM CYGNSS vector winds. The VAM CYGNSS vector wind error is  
228 taken to be the simulated CYGNSS observation error determined by the E2ES plus the RMS  
229 VAM error compared to observations (i.e., root mean square of CYGNSS wind speed minus VAM  
230 analysis wind speed) to account for the influence of the VAM analysis on observation error.  
231 The VAM analysis cost function balances the fit to observations with a minimum departure

232 from the background, so the RMS VAM error implicitly includes an estimate of background  
233 error.

234

### 235 2.3 Data Assimilation and Forecast Model

236 Since a global modeling system is heavily parameterized and cannot sufficiently resolve the  
237 small scales that are major contributors to the TC rapid intensification processes, a regional  
238 model specifically developed for TCs is used in this study. HWRF is used specifically to be  
239 consistent with the goals of Hurricane Forecast Improvement Project (Gall et al., 2013) and  
240 because the research version closely parallels the operational version. This approach allows us  
241 to assess the impact of new observing systems through improved HWRF initial conditions (IC),  
242 and is a similar set up used by Atlas et al. (2015b) to investigate the potential impact of an  
243 Optical Auto-covariance Wind Lidar (OAWL) on TC prediction. In our experiments, we use the  
244 2012 version of the operational National Centers for Environmental Prediction (NCEP)  
245 Hurricane-WRF (HWRF) data assimilation (DA) system. The HWRF model parameterizations  
246 include the Global Forecast System (GFS) planetary boundary layer scheme, the new Simplified  
247 Arakawa-Schubert cumulus scheme (only for the parent domain since convection is explicit in  
248 the nested domain), the Ferrier microphysics scheme, and the Geophysical Fluid Dynamics  
249 Laboratory (GFDL) scheme for shortwave and longwave radiation. This version (v3.5)  
250 (Tallapragada et al., 2013; Atlas et al., 2015c) is configured in our experiments with a fixed 9-km  
251 parent domain and a 3-km nested storm-following domain (cf. Fig. 4). In the HWRF DA system,  
252 NCEP's GSI 3-dimensional variational (3DVar) scheme assimilates the observations. Quality  
253 control (QC) follows GSI's practice of gross outlier removal by comparison with background

254 values, and CYGNSS data are treated as ship observations for QC purposes. Data assimilation is  
255 performed on the 9-km domain only, with no vortex relocation.

256

### 257 3. Experimental design

258 Nine experiments varying the use of the CYGNSS observations and the frequency of the DA  
259 cycling interval are carried out within the OSSE system to assess the simulated impact of  
260 CYGNSS observations on hurricane analysis and forecasting. First, a control DA experiment  
261 (CTRL) assimilates standard conventional data that are routinely assimilated in the 2012 GFS  
262 Data Assimilation System (GDAS), including radiosondes, atmospheric motion vectors, and  
263 numerous satellite-based observations (see section 2.2.2), but no CYGNSS observations. This is  
264 followed by an experiment where CYGNSS wind speeds are added to the control (CYG), and an  
265 experiment where VAM CYGNSS wind vectors are added to the control (VAM). Each of these  
266 OSSEs is conducted at three data assimilation frequencies: 6-hourly, 3-hourly, and 1-hourly.  
267 (The numeral “6”, “3”, or “1” is added to the experiment names to denote cycling frequency;  
268 see Table 1.) Note that all simulated observations are binned/grouped by time at these  
269 frequencies, i.e., +/- 3, +/-1.5 and +/-0.5 h time windows around the DA analysis times,  
270 respectively. For convenience, in the text, we will refer to all the CTRL, CYG and VAM  
271 experiments collectively as EXP; CTRL6, CYG6 and VAM6 experiments collectively as EXP6, and  
272 similarly for EXP3 and EXP1.

273

274 The nine experiments and the average number of CYGNSS data assimilated in each DA cycle are  
275 listed in row 3 and 4 of Table 1. Although the total number of observations is the same, these

276 are divided into smaller chunks with increased cycling frequency. Also, the number of  
277 assimilated variables doubles for the VAM experiments, since there are two wind components  
278 (u- and v-wind) for each simulated CYGNSS wind speed in the CYG experiments. All of the  
279 experiments are initialized at 0000 UTC 1 August 2005. GFS global control OSSE analyses  
280 described by Casey et al. (2016) are used to provide initial and lateral boundary conditions.  
281 Cycling is performed through 0000 UTC 5 August, for a total of 16, 32, and 96 analyses for  
282 experiments with 6-, 3-, and 1-h cycles, respectively. A five-day HWRF forecast is initialized  
283 every 6 hours in all experiments. Each experiment is then verified against the HNR1. Forecast  
284 initial times before 0600 UTC 2 August are discarded to eliminate the effects of model  
285 adjustment to the cold start from the global analysis. Error statistics reported below from  
286 these nine OSSE experiments are compared using the final twelve forecasts in the experiment  
287 period (i.e., with initialization times every 6 h from 0600 UTC 2 August to 0000 UTC 5 August).

288

#### 289 4. OSSE Results

290 The results of the experiments described in the previous section are presented here in three  
291 parts: (1) statistical summaries of the errors in TC track and intensity, (2) domain-wide errors,  
292 and (3) physical interpretations of the analyses and forecasts of the 10-meter wind field.

293

##### 294 4.1 Assessment of TC track and intensity errors

295 To evaluate and compare the effect of simulated CYGNSS wind speed and VAM CYGNSS wind  
296 vectors, tropical cyclone metrics are calculated and compared to HNR1 values (truth). Those  
297 metrics are: storm center position, minimum sea-level pressure (MSLP; hPa) and the maximum

298 wind speed (kt ; Gall et al 2013). For each 5-day forecast within a given OSSE experiment  
299 (forecasts are started every 6 hours at synoptic times), error metrics are computed with respect  
300 to the HNR1 every six hours. Error in all cases is defined as experiment minus the truth (EXP-  
301 HNR1). Mean and standard deviation of error are computed from twelve forecasts (N=12) at  
302 each forecast lead time to 96 hours. (However, N is reduced for 108 and 120 h forecasts  
303 because some of the later verification times move the HNR1 hurricane close to the boundaries  
304 of our regional OSSE domain. For this reason, we show results from here forward for 0-96 hour  
305 forecasts.) Note that we calculate mean error, not mean absolute error. Nevertheless, track  
306 errors are always positive. Also, since the HWRF OSSE hurricanes are uniformly less intense  
307 than the HNR1 hurricane, all errors are positive (for MSLP) or negative (for maximum wind  
308 speed). So, in an absolute sense, the results shown are equal to mean absolute error. Note that  
309 while twelve is not a large number of forecasts for assessing statistical significance and these  
310 forecasts are all during the lifetime of a single simulated hurricane, the average performance  
311 does provide an indication of the variation of error over the forecast hours and between OSSE  
312 experiments.

313

314 The first row of Fig. 5 (a-c) shows the hurricane track error for each cycling frequency (6-, 3- and  
315 one-hourly). In each panel, the mean and standard deviation of the track errors with respect to  
316 the HNR1 are plotted as a function of forecast hour for CTRL, CYG and VAM experiments.

317 Overall, the track errors among the experiments for any given cycling frequency are quite  
318 similar, i.e., forecast error growth dominates CYGNSS impact. All OSSE experiments and cycling  
319 frequencies produce similar position errors for 1-3-day forecasts (0-72 h), but EXP6 errors are

320 smaller than EXP3 and EXP1 errors for 3-4-day forecasts. An inverse relationship between  
321 cycling frequency and observation data coverage means that the 3-4-day track errors are  
322 increased for EXP3 and EXP1 compared to EXP6. The large-scale environment is better  
323 characterized by the increased data coverage of 6-hourly cycling. Initial position error (forecast  
324 hour 0) is smallest for EXP3 (Fig 5b; ~ 50 km). Judging from the overlap of one-standard-  
325 deviation bounds, analysis errors are likely not statistically significant. The differences in  
326 forecast track error statistics by cycling frequency are large enough to explore the statistical  
327 significance between different DA cycling intervals (see discussion of Fig. 6 below). For these  
328 OSSE experiments based on the HNR1 case, CYGNSS data do not seem to improve or degrade  
329 the forecast track, but the differences in track error are sensitive to cycling frequency.

330

331 The second row of Fig. 5 (d-f) is similar in presentation to the first row, but for MSLP. As with  
332 track error, there are significant differences between experiments using different cycling  
333 frequencies. But unlike track error, EXP3 produces the lowest overall MSLP errors. For  
334 example, mean MSLP analysis errors (forecast hour zero) are 19-22 hPa for EXP6, 11-13 hPa for  
335 EXP3 and 13-17 hPa for EXP1. The standard deviation of MSLP forecast errors tends to decrease  
336 for all experiments, indicative of the forecast model consistently spinning-up initially weak  
337 storms. Notice that unlike track error, MSLP error is sensitive to both cycling frequency and the  
338 assimilation of CYGNSS data. For all cycling frequencies, the VAM OSSE experiments have the  
339 lowest MSLP errors compared to CTRL and CYG experiments over forecast hours 0-48. The  
340 positive impact of CYGNSS data evident in these average MSLP error statistics is large enough to  
341 explore statistical significance further (see discussion of Fig. 7 below).

342

343 The third row of Figure 5 (g-i) shows the error in maximum wind speed for all OSSE  
344 experiments. The monotonic reduction in maximum wind speed error (i.e., less negative) for all  
345 experiments during forecast hours 0-48 is another reflection of the forecast model consistently  
346 spinning-up initially weak storms. The maximum wind speed is closely tied to MSLP through the  
347 wind-pressure relationship (Knaff and Zehr 2007). Both metrics reflect hurricane intensity. Like  
348 the MSLP errors already discussed, maximum wind speed errors are smallest for EXP3,  
349 particularly during the start (out to 48 h) of the forecasts. This indicates that differences in  
350 these hurricane error statistics in our OSSE study are primarily due to cycling frequency.  
351 However, as with MSLP errors, assimilation of CYGNSS observations reduces maximum wind  
352 speed analysis and forecast errors through forecast hours 0-48 for all cycling frequencies by 0-8  
353 kt.

354

355 The results in Fig. 5 point to potentially important impacts of assimilating simulated CYGNSS  
356 observations on hurricane intensity (i.e., reduced MSLP and maximum wind speed errors) and  
357 cycling frequency. To explore this further, the statistical significance of differences in forecast  
358 error between OSSE experiments is investigated. First, the influence of cycling frequency is  
359 shown in Figure 6 using the three CTRL OSSE experiments. CTRL3 and CTRL1 experiments are  
360 investigated, using CTRL6 errors as a common baseline. Using the CTRL experiments removes  
361 the influence of simulated CYGNSS observations from the evaluation of cycling frequency. MSLP  
362 error differences (Fig. 6a) show that assimilation every 3 h (CTRL3) improves forecast MSLP by  
363 0-10 hPa during the first 24 hours compared to 6-hourly cycling (CTRL6). To assess significance,

364 the 95<sup>th</sup> percentile confidence interval (CI) from a two-sided paired t-test is plotted with gray  
365 semi-transparent shading. The 1-sided 95% confidence intervals are also plotted as light dotted  
366 or dash-dotted lines. Where the 1-sided CI lines are greater than zero, the mean experiment  
367 MSLP error is less than CTRL6 error with greater than 95% confidence. Fig. 6a shows that the  
368 CTRL1 experiment improvements are marginally significant at the 95% confidence level for  
369 forecast hours 0-60. But the improvement by assimilating every 3 hours is larger than in  
370 experiment CTRL1 during forecast hours 0-24, and with 95% significant difference between  
371 CTRL6 and CTRL3. The improvement from assimilation at at 1- or 3-h intervals after 48 hours  
372 reduces to near zero for the remainder of the forecast period

373

374 The statistical significance of impacts on forecast maximum wind speed for different cycling  
375 frequencies are shown in Fig. 6b. The figure can be interpreted similarly to Fig. 6a and shows  
376 results similar to MSLP. Therefore, forecasts of both MSLP and maximum wind speed are most  
377 accurate with 3-hourly cycling and the improvements are statistically significant for at least the  
378 first 24 hours.

379

380 Next, the influence of CYGNSS data on the 3-hourly cycling experiments is shown in Figure 7.  
381 CYG3 and VAM3 experiments are investigated, using CTRL3 errors as a common baseline. Figure  
382 7 shows the difference between CYG3/VAM3 experiment errors and CTRL3 errors, i.e., CTRL3-  
383 EXP3, for MSLP and maximum wind speed. MSLP error differences (Fig. 7a) indicate that  
384 assimilation of CYGNSS data (both in scalar and vector form; CYG3 vs. VAM3, respectively)  
385 improves the forecast MSLP by 2-5 hPa during the first 48 hours. To assess significance, the 95<sup>th</sup>

386 percentile confidence interval (CI) from a two-sided paired t-test is plotted with light blue and  
387 light orange semi-transparent shading. Since the OSSE forecast hurricanes are uniformly less  
388 intense than HNR1, a more appropriate hypothesis is that the CYGNSS observations increase  
389 the intensity of the analyzed and forecast hurricane. There the 1-sided 95% confidence intervals  
390 are also plotted as dotted lines. Where the dotted, 1-sided CI lines are greater than zero, the  
391 mean experiment MSLP error is less than CTRL3 error with 95% confidence. Fig. 7a shows that  
392 the VAM3 experiment improvements are marginally significant at the 95% confidence level for  
393 forecast hours 0-48. The improvement by assimilating VAM3 vectors is somewhat larger than  
394 in experiment CYG3 during forecast hours 0-36, and with 95% significant difference between  
395 forecast hours 24-36. The improvement from assimilation of VAM CYGNSS vectors after 48  
396 hours reduces to near zero for the remainder of the 5-day forecast period, whereas the  
397 improvement from the assimilation of CYGNSS wind speed continues in the forecasts until 96  
398 hours. But the reduction in error in the CYG3 forecasts between hours 48-96 is only statistically  
399 significant with 95% confidence at forecast hour 72.

400

401 The statistical significance of impacts from assimilating CYGNSS observations on forecast  
402 maximum wind speed are shown in Fig. 7b. The figure can be interpreted similarly to Fig. 7a.  
403 Because intensity in terms of maximum wind speed has the opposite sense of intensity in terms  
404 of MSLP (see above), improvements in CYG3 and VAM3 forecasts with respect to CTRL3 appear  
405 as mean error differences less than zero. Therefore, where the 1-sided CI lines (dotted lines)  
406 are less than zero, the mean experiment maximum wind speed error is less than CTRL3 error  
407 with 95% confidence. The average reduction in maximum wind speed error from assimilation of

408 CYGNSS observations is 2-6 kt over forecast hours 0-54. The VAM3 error differences from  
409 CTRL3 are significant at the 95% level for forecast hours 0-54.

410

#### 411 4.2 Domain-wide errors

412 Figure 8 shows the domain-wide error statistics for 10-meter wind speeds with respect to the  
413 HNR1 10-meter winds. Given that the 9-km domain dimensions are 411 x 705, and that there  
414 are 12 forecasts, the RMS error (square root of the mean squared vector wind difference) at  
415 each 6-h forecast interval is the result of approximately 3.5 million wind speed differences (EXP  
416 - HNR1). Notice that the RMS errors are generally quite small, increasing from 1-2 kt in the  
417 analyses (forecast hour 0) to 3-4 kt for 5-day forecasts. The standard deviation of those errors  
418 also increases from 0.25 kt to 1 kt. As with the error statistics presented in Fig. 5, the EXP3 have  
419 the lowest errors at analysis times. The effect of CYGNSS data can be seen over the first 0-24  
420 forecast hours on a domain-wide basis. The RMS error in the analyzed fields is reduced by  
421 small but consistent amounts (0.1 – 0.25 kt as forecast time increases) by the assimilation of  
422 CYGNSS data (i.e., compared to CTRL), with the largest reductions occurring in the 6-hourly and  
423 1-hourly cycling experiments at least in part since CTRL6 and CTRL1 errors are larger than CTRL3  
424 error. Improvements similar to those in the 10-meter, domain-averaged winds owing to  
425 CYGNSS data can be seen in other upper level fields (e.g., 850 hPa temperature, 500 hPa  
426 heights; not shown).

427

428 Figure 9 shows the absolute integrated kinetic energy (IKE) differences (errors) between the  
429 OSSE experiments and HNR1, arranged by cycling frequency as in Fig. 8. In Fig. 9, IKE is the

430 domain integral of the squared 10-m wind vector, scaled into energy units (Powell and  
431 Reinhold, 2007). Thus, IKE accumulates the energy of a 2D wind field at a given time to a single,  
432 scalar estimate of total energy. The IKE differences by experiment and by DA cycling frequency  
433 mirror the results presented in Figs. 5 and 7 for MSLP error, maximum wind error and domain-  
434 wide 10-meter wind error. That is, 3-hourly DA cycling produces the lowest IKE error for CTRL,  
435 CYG and VAM experiments, and the assimilation of CYGNSS data, whether wind speed or VAM  
436 CYGNSS vector data, reduces the IKE error at all cycling frequencies which is in agreement with  
437 results presented in McNoldy et al. (2016). As seen in the domain-wide errors in Fig. 8, the  
438 error reduction from the assimilation of CYGNSS data is largest in the 6-hourly and hourly  
439 cycling experiments at least in part since CTRL6 and CTRL1 errors are larger than CTRL3 error.

440

#### 441 4.3 10-meter hurricane wind field

442 The distribution of surface wind vectors around a hurricane is its dynamic footprint on the  
443 ocean surface. It reflects the structure of the low-level wind field and controls interaction with  
444 the ocean surface, including storm surge, surface fluxes, the wave field, and ocean mixed-layer  
445 depth. Next, visualizations of 10-meter wind fields from the HNR1 and OSSE experiments  
446 illustrate the impact of CYGNSS data

447

448 Given the significance of the improvement in 0-48-h intensity forecasts shown in the previous  
449 section, Figures 10 and 11 illustrate the physical impacts of assimilation of CYGNSS data on 24-  
450 hour forecasts of the 10-meter wind field. For the period and geographic region of our study,  
451 the entire hurricane circulation is sampled by CYGNSS during the two, 3-hourly DA cycles each

452 day at 1500 and 1800 UTC. Therefore, 5-day forecasts starting at 1800 UTC on any day during  
453 the OSSE experiments have the benefit of one or two recent 3-hourly DA cycles with  
454 assimilation of CYGNSS data in or near the inner core of the tropical cyclone. So, 24-h forecasts  
455 starting at 1800 UTC should show the clearest benefit from assimilation of these data.

456

457 Figure 10 shows 10-meter wind speed fields from the HNR1 (9-km domain) and three 24-hour  
458 forecasts from the 9-km domain of OSSE experiments CTRL3, CYG3 and VAM3, all valid at 1800  
459 UTC August 4. The fields are instantaneous values and are therefore subject to fluctuation from  
460 time step to time step. For example, the maximum wind speed can change location and  
461 intensity from model time-step to time-step. Nevertheless, the pattern of the 10-meter wind  
462 speed field gives a good overall indication of intensity and shows storm asymmetries. The HNR1  
463 wind speed maximum of  $52.8 \text{ m s}^{-1}$  is more closely approximated by CYG3 and VAM3 24-hour  
464 forecasts (maximum wind speeds of  $49.8$  and  $51.6 \text{ m s}^{-1}$ , respectively) than by CTRL3 ( $47.0 \text{ m s}^{-1}$ ).  
465 Also, the closed annulus of winds greater than  $40 \text{ m s}^{-1}$  in HNR1 is most closely  
466 approximated by the 24-hour CYG3 forecast. Neither the CTRL3 nor VAM3 24-hour forecast  
467 wind fields have wind speeds greater than  $40 \text{ m s}^{-1}$  in all quadrants as in the HNR1 and CYG3  
468 forecast. Thus, the 24-hour forecast wind fields in both experiments that assimilate CYGNSS  
469 data (CYG3 and VAM3) are improved but in different aspects compared to the CTRL3 forecast.

470

471 Figure 11 shows a comparison of OSSE 24-h forecast wind field to the HNR1 wind field but valid  
472 1800 UTC August 5, a day later than in Fig. 10. In this comparison, the VAM3 forecast is closest  
473 in intensity and structure to the HNR1 wind field. Note that the CYG3 forecast wind field is not

474 as intense or as well structured as the CTRL3 forecast wind field. At other analysis times,  
475 assimilation of CYGNSS data when the hurricane is only partially covered can produce  
476 asymmetries in the resulting GSI 3DVar analyses in both CYG3 and VAM3 experiments (not  
477 shown). The issue of partial sampling of tropical systems by space-based instruments that  
478 measure ocean surface winds (passive microwave and scatterometers) has long been a  
479 challenge for DA systems. However, in our OSSE experiments, the asymmetries introduced by  
480 the assimilation of simulated CYGNSS wind speed (CYG3) are often stronger and more  
481 disturbing to the structure of the surface wind field than the assimilation of VAM CYGNSS winds  
482 (VAM3). The more complete set of information presented to the DA system as VAM CYGNSS  
483 winds is likely the reason that these winds produce consistently better analyses and 0-48 hour  
484 forecasts compared to CYG experiments. This is one explanation for the differences between  
485 CYG3 and VAM3 0-48 hour forecast errors presented in Fig. 7 (Section 4.1).

486

## 487 5. Summary and concluding remarks

488

489 The potential value of observations to be collected by the NASA Cyclone Global Navigation  
490 Satellite System (CYGNSS) for hurricane analysis and forecasting is explored in a simulation  
491 study. Since vector winds have more information content than scalar winds, two approaches to  
492 assimilating the CYGNSS observations were tested: CYGNSS winds were assimilated as scalar  
493 wind speeds and as wind vectors determined by the VAM (as described by L17). Because TCs  
494 can evolve rapidly, results from three different DA cycle intervals (1-, 3-, and 6-hourly) were  
495 compared to assess CYGNSS impact.

496

497 The OSSE experiment results on the 9-km domain are evaluated with respect to the HNR1 9-km  
498 domain. A combination of statistical evaluations of analysis and forecast errors and  
499 phenomenological evaluations of the OSSE hurricane 10-meter wind fields demonstrate a  
500 number of consistent findings. Overall, the results show that impacts of assimilating simulated  
501 CYGNSS data on the analysis and forecasts are positive and that the OSSE system performance  
502 is sensitive to cycling frequency. Analysis and forecast errors for all experiments (CTRL, CYG and  
503 VAM) are lowest for 3-hourly DA cycling, and lower than 6-hourly and 1-hourly errors with  
504 statistical significance greater than 95% for 0-36h forecast lead times. This result demonstrates  
505 that the interaction between hurricane forecasts in the HWRF model and 3-hourly application  
506 of GSI 3DVar are the most beneficial to the maintenance of a balanced cyclone during DA  
507 cycling . Therefore, the following summary of results focuses on 3-hourly DA cycling  
508 experiments, though similar results hold for all cycling frequencies.

509

510 For the 3-hourly DA cycling OSSE experiments, CYGNSS data improve the forecast intensity of  
511 the simulated hurricane over the first 48 h by 2-5 hPa for minimum sea-level pressure and by 2-  
512 6 kt for maximum wind speed compared to experiment CTRL3. These improvements are  
513 statistically significant at the 95% confidence level for VAM3 experiment, and at a 90%  
514 confidence level for the CYG3 experiment. There is no statistically significant reduction or  
515 increase in track error for OSSE experiments CYG3 or VAM3 compared to CTRL3. For forecast  
516 hours 48-96, the intensity improvement in the VAM3 experiment is reduced to near zero, and  
517 the intensity improvement in CYG3 experiment is still positive but with lower statistical

518 confidence (i.e., < 95%). This improvement in forecasts due to CYGNSS observations is also  
519 quantified as a reduction of integrated kinetic energy (IKE) error in all experiments that  
520 assimilate simulated CYGNSS data compared to CTRL experiments. From examples of 24-hour  
521 HWRF forecasts of the 10-meter surface winds along with the validating HNR1 wind fields, the  
522 structure of the inner core 10-meter wind field in CYG and VAM experiment forecasts is  
523 improved compared to CTRL experiments.

524

525 These results suggest that for forecast hours 0-36, assimilation of VAM CYGNSS vectors  
526 improves the intensity and structure of the 10-meter wind field in HWRF forecasts more than  
527 assimilation of CYGNSS wind speed alone. When GSI 3DVar is applied to cases with partial  
528 coverage of the hurricane circulation by simulated CYGNSS wind observations, assimilation of  
529 CYGNSS wind speed routinely produces larger asymmetries in the analyzed hurricane wind field  
530 compared to assimilating VAM CYGNSS vectors. The evidence for this can be seen in the  
531 reduction of mean MSLP and maximum wind speed errors for VAM experiments compared to  
532 CYG experiments for forecast hours 0-36 hours. Further examples in L17 show that the VAM  
533 wind vectors are dynamically consistent with the background. Greater impact from CYGNSS is  
534 anticipated when plans are realized to integrate the VAM into the HWRF DA system as a pre-  
535 processor for CYGNSS observations (L17). It should be noted that using HWRF short-term  
536 forecasts as backgrounds for VAM analyses will bias VAM CYGNSS vectors toward HWRF model  
537 solutions, including model errors. However, for the small spatial scales in the wind field near  
538 the centers of TCs, it is arguable that no better choice of backgrounds for VAM wind vector  
539 analyses exists for use in near real-time operations.

540

541 The most important limitations of the present study are that static background error covariance  
542 (BEC) is used and that this is a single case study. Since TCs are highly structured phenomena,  
543 the true BECs are complex and poorly approximated by the static BECs used in this study.  
544 Ensemble and hybrid DA methods should be used in future OSSEs and OSEs to overcome this  
545 limitation. A comparison of multiscale GSI-based EnKF and 3DVar assimilation shows that the  
546 EnKF produces improved analysis and forecasts primarily due to local, flow-dependent  
547 background error covariances and cross-variable correlation (Johnson et al. 2015). One storm is  
548 clearly too small of a sample size to draw any general results, and a much larger sample of  
549 simulated TCs in different ocean basins is required to generate more robust error statistics. This  
550 study should be extended to multiple TCs using real data. The 2017 hurricane season provides  
551 the first opportunity to systematically observe tropical cyclones with the CYGNSS constellation.  
552 During this period, the authors plan to investigate the impact of real CYGNSS data, assimilating  
553 both scalar wind speed and VAM CYGNSS vectors, in Observing System Experiments (OSEs) that  
554 parallel HWRF operations.

555

## 556 Acknowledgments

557 This study was supported by NOAA---directly and through the Cooperative Agreement  
558 NA15OAR4320064 for the Cooperative Institute for Marine and Atmospheric Studies (CIMAS)---  
559 and by NASA through Award NNL13AQ00C. We thank Christopher Ruf at the University of  
560 Michigan and the CYGNSS Science Team for the simulated CYGNSS datasets, the NOAA Office of  
561 Weather and Air Quality for funding the initial development of the regional OSSE framework,

562 the NOAA Hurricane Forecast Improvement Project for computing resources, the  
563 Developmental Testbed Center for the GSI and HWRF code and support, Sean Casey at  
564 CIMAS/AOML for providing the GFS Control data, and David Nolan at the University of Miami  
565 for providing the WRF nature run dataset.

## 566 References

567 Aberson, S. D., M. L. Black, R. A. Black, J. J. Cione, C. W. Landsea, F. D. Marks, and R. W. Burpee,  
568 2006: Thirty years of tropical cyclone research with the NOAA P-3 aircraft. *Bull. Amer.*  
569 *Meteor. Soc.*, 87, 1039–1055, doi:10.1175/bams-87-8-1039.

570 Andersson, E. and M. Masutani, 2010: Collaboration on observing system simulation  
571 experiments (joint OSSE). *ECMWF Newsletter*, (123), 14–16.

572 Atlas, R., 1997: Atmospheric observations and experiments to assess their usefulness in data  
573 assimilation. *J. Meteor. Soc. Japan*, 75 (1B), 111–130.

574 Atlas, R., L. Bucci, B. Annane, R. Hoffman, and S. Murillo, 2015a: Observing system simulation  
575 experiments to assess the potential impact of new observing systems on hurricane  
576 forecasting. *Mar. Tech. Soc. J.*, 49 (6), 140–148, doi:10.4031/MTSJ.49.6.3. Special issue,  
577 Evolution of Marine Technologies: Commemorating the 50th Anniversary of the MTS  
578 Journal, guest edited by Donna Kocak.

579 Atlas, R., R. N. Hoffman, J. Ardizzone, S. M. Leidner, J. C. Jusem, D. K. Smith, and D. Gombos,  
580 2011: A cross-calibrated, multi-platform ocean surface wind velocity product for

581 meteorological and oceanographic applications. *Bull. Amer. Meteor. Soc.*, 92 (2), 157–  
582 174, doi:10.1175/2010bams2946.1.

583 Atlas, R., R. N. Hoffman, S. C. Bloom, J. C. Jusem, and J. Ardizzone, 1996: A multiyear global  
584 surface wind velocity data set using SSM/I wind observations. *Bull. Amer. Meteor. Soc.*,  
585 77 (5), 869–882.

586 Atlas, R., V. Tallapragada, and S. Gopalakrishnan, 2015b: Advances in tropical cyclone intensity  
587 forecasts. *Mar. Tech. Soc. J.*, 49 (6), 149–160, doi:10.4031/MTSJ.49.6.2. Special issue,  
588 Evolution of Marine Technologies: Commemorating the 50th Anniversary of the MTS  
589 Journal, guest edited by Donna Kocak.

590 Atlas, R., et al., 2001: The effects of marine winds from scatterometer data on weather analysis  
591 and forecasting. *Bull. Amer. Meteor. Soc.*, 82 (9), 1965–1990, doi:10.1175/1520-  
592 0477(2001)082<1965:TEOMWF>2.3.CO;2.

593 Atlas, R., et al., 2015c: Observing system simulation experiments (OSSEs) to evaluate the  
594 potential impact of an optical autocovariance wind lidar (OAWL) on numerical weather  
595 prediction. *J. Atmos. Oceanic Technol.*, 32 (9), 1593–1613, doi:10.1175/JTECH-D-15-  
596 0038.1.

597 Candy, B., S. J. English, and S. J. Keogh, 2009: A comparison of the impact of QuikScat and  
598 WindSat wind vector products on Met Office analyses and forecasts. *IEEE Trans. Geosci.*  
599 *Remote Sens.*, 47 (6), 1632–1640.

600 Casey, S. P. F., et al., 2016: Geostationary hyperspectral infrared constellation: Global observing

601 system simulation experiments for five Geo-HSS instruments. *20th Conference on*  
602 *Integrated Observing and Assimilation Systems for the Atmosphere, Oceans, and Land*  
603 *Surface (IOAS-AOLS)*, American Meteorological Society, Boston, MA, New Orleans, LA,  
604 paper J7.4. Recorded presentation: Available online at  
605 <https://ams.confex.com/ams/96Annual/webprogram/Paper283540.html>.

606 Claziria, M. P. and V. Zavorotny, 2015: Algorithm theoretical basis document level 2 wind speed  
607 retrieval. Document 148-0138, University of Michigan. 95 pp.

608 Entekhabi, D., E. Njoku, P. O'Neill, K. Kellogg, K., W. Crow, W. Edelstein, J. Entin, S. Goodman, T.  
609 Jackson, J. Johnson, J. Kimball, J. Peipmeier, R. Koster, K. McDonald, M. Moghaddam, M.  
610 S. Moran, R. Reichle, J. Shi, M. Spencer, and S. Thurman, S., "The Soil Moisture Active  
611 and Passive (SMAP) Mission," *Proceedings of the IEEE*, 98(5), pp. 704–716, 2010

612 Errico, R. M., Yang, R. , Privé, N. C., Tai, K. , Todling, R. , Sienkiewicz, M. E. and Guo, J. (2013),  
613 Development and validation of observing-system simulation experiments at NASA's  
614 Global Modeling and Assimilation Office. *Q.J.R. Meteorol. Soc.*, 139: 1162-1178.  
615 doi:10.1002/qj.2027

616 Gall, R., J. Franklin, F. Marks, E. N. Rappaport, and F. Toepfer, 2013: The hurricane forecast  
617 improvement project. *Bull. Amer. Meteor. Soc.*, 94 (3), 329–343, doi:10.1175/bams-d-  
618 12-00071.1.

619 Gopalakrishnan, S. G., S. Goldenberg, T. Quirino, X. Zhang, F. Marks, Jr., K.-S. Yeh, R. Atlas, and  
620 V. Tallapragada, 2012: Toward improving high-resolution numerical hurricane

621 forecasting: Influence of model horizontal grid resolution, initialization, and physics.  
622 *Wea. Forecasting*, 27 (3), 647–666, doi:10.1175/WAF-D-11-00055.1.

623 Hock, T. F. and J. L. Franklin, 1999: The NCAR GPS dropwindsonde. *Bull. Amer. Meteor. Soc.*, 80  
624 (3), 407–420.

625 Hoffman, R., 1982: SASS wind ambiguity removal by direct minimization. *Mon. Wea. Rev.*, 110  
626 (5), 434–445.

627 Hoffman, R. N., 1984: SASS wind ambiguity removal by direct minimization. II: Use of  
628 smoothness and dynamical constraints. *Mon. Wea. Rev.*, 112 (9), 1829–1852.

629 Hoffman, R. N. and R. Atlas, 2016: Future observing system simulation experiments. *Bull. Amer.*  
630 *Meteor. Soc.*, 97 (9), 1601–1616, doi:10.1175/BAMS-D-15-00200.1.

631 Hoffman, R. N., S. M. Leidner, J. M. Henderson, R. Atlas, J. V. Ardizzone, and S. C. Bloom, 2003:  
632 A two-dimensional variational analysis method for NSCAT ambiguity removal:  
633 Methodology, sensitivity, and tuning. *J. Atmos. Oceanic Technol.*, 20 (5), 585–605.

634 Johnson, A., X. Wang, J. R. Carley, L. J. Wicker, and C. Karstens, 2015: A comparison of  
635 multiscale GSI-based EnKF and 3DVar data assimilation using radar and conventional  
636 observations for midlatitude convective-scale precipitation forecasts. *Mon. Wea. Rev.*,  
637 143 (8), 3087–3108.

638 Knaff, J. A. and R. M. Zehr, 2007: Reexamination of tropical cyclone wind-pressure relationships.  
639 *Wea. Forecasting*, 22 (1), 71–88, doi:10.1175/WAF965.1.

640 Komjathy, A., M. Armatys, D. Masters, P. Axelrad, V. Zavorotny, and S. Katzberg, 2004: Retrieval  
641 of ocean surface wind speed and wind direction using reflected GPS signals. *J. Atmos.*  
642 *Oceanic Technol.*, 21 (3), 515–526, doi:10.1175/1520-  
643 0426(2004)021<0515:ROOSWS>2.0.CO;2.

644 Leidner, S. M., B. Annane, B. McNoldy, R.N. Hoffman, and R. Atlas, 2017: Variational Analysis  
645 of Simulated Ocean Surface Winds from the Cyclone Global Navigation Satellite System  
646 (CYGNSS) and Evaluation using a Regional OSSE, submitted to Journal of Atmospheric  
647 and Oceanic Technology, manuscript JTECH-D-17-0136.

648

649 Leidner, S. M., L. Isaksen, and R. N. Hoffman, 2003: Impact of NSCAT winds on tropical cyclones  
650 in the ECMWF 4D-Var assimilation system. *Mon. Wea. Rev.*, 131 (1), 3–26,  
651 doi:10.1175/1520-0493(2003)1314<0003:ionwot>2.0.co;2.

652 McNoldy, B., B. Annane, S. Majumdar, J. Delgado, L. Bucci, and R. Atlas, 2017: Impact of  
653 assimilating CYGNSS data on tropical cyclone analyses and forecasts in a regional OSSE  
654 framework. *Mar. Tech. Soc. J.*, 51 (1), 7–15, doi:10.4031/MTSJ.51.1.1.

655 McNoldy, B. D., B. Annane, J. Delgado, L. Bucci, R. Atlas, S. J. Majumdar, M. Leidner, and R. N.  
656 Hoffman, 2016: Impact of CYGNSS data on tropical cyclone analyses and forecasts in a  
657 regional OSSE framework. *20th Conference on Integrated Observing and Assimilation*  
658 *Systems for the Atmosphere, Oceans, and Land Surface (IOAS-AOLS)*, American  
659 Meteorological Society, Boston, MA, New Orleans, LA, paper J6.6. Recorded

660 presentation: Available online at  
661 <https://ams.confex.com/ams/96Annual/webprogram/Paper285158.html>.

662 Nolan, D. S., R. Atlas, K. T. Bhatia, and L. R. Bucci, 2013: Development and validation of a  
663 hurricane nature run using the joint OSSE nature run and the WRF model. *Journal of*  
664 *Advances in Modeling Earth Systems*, 5 (2), 382–405, doi:10.1002/jame.20031.

665 O’Brien, A., 2014: CYGNSS end-to-end simulator technical memo. Document 148-0123,  
666 University of Michigan. 23 pp. Available online at [http://clasp-](http://clasp-research.engin.umich.edu/missions/cygnss/reference/148-0123%20CYGNSS%20E2ES%20EM.pdf)  
667 [research.engin.umich.edu/missions/cygnss/reference/148-0123 CYGNSS E2ES EM.pdf](http://clasp-research.engin.umich.edu/missions/cygnss/reference/148-0123%20CYGNSS%20E2ES%20EM.pdf).

668 Powell, M. D. and T. A. Reinhold, 2007: Tropical cyclone destructive potential by integrated  
669 kinetic energy. *Bull. Amer. Meteor. Soc.*, 88 (4), 513–526, doi:10.1175/bams-88-4-513.

670 Rappaport, E. N., et al., 2009: Advances and challenges at the National Hurricane Center. *Wea.*  
671 *Forecasting*, 24 (2), 395–419, doi:10.1175/2008waf2222128.1.

672 Rogers, R., P. Reasor, and S. Lorsolo, 2013: Airborne Doppler observations of the inner-core  
673 structural differences between intensifying and steady-state tropical cyclones. *Mon.*  
674 *Wea. Rev.*, 141 (9), 2970–2991, doi:10.1175/MWR-D-12-00357.1.

675 Ruf, C. S., et al., 2016a: New ocean winds satellite mission to probe hurricanes and tropical  
676 convection. *Bull. Amer. Meteor. Soc.*, 97 (3), 385–395, doi:10.1175/BAMS-D-14-00218.1.

677 Ruf, C., P. Chang, M.P. Clarizia, S. Gleason, Z. Jelenak, J. Murray, M. Morris, S. Musko, D. Posselt,  
678 D. Provost, D. Starckenburg, V. Zavorotny, 2016b: CYGNSS Handbook, Ann Arbor, MI,

679 Michigan Pub., ISBN 978-1-60785-380-0, 154 pp, 1 Apr 2016.

680 Schulz, E. W., J. D. Kepert, and D. J. M. Greenslade, 2007: An assessment of marine surface  
681 winds from the Australian Bureau of Meteorology numerical weather prediction  
682 systems. *Wea. Forecasting*, 22 (3), 613–636, doi:10.1175/WAF996.1.

683 Tallapragada, V., et al., 2013: Hurricane Weather Research and Forecasting (HWRF) model:  
684 2013 scientific documentation. Tech. rep., Developmental Testbed Center (DTC).  
685 Version 3.5a, 137 pp. Available online at  
686 <http://www.dtcenter.org/HurrWRF/users/docs/>.

687 Uhlhorn, E. W., P. G. Black, J. L. Franklin, M. Goodberlet, J. Carswell, and A. S. Goldstein, 2007:  
688 Hurricane surface wind measurements from an operational stepped frequency  
689 microwave radiometer. *Mon. Wea. Rev.*, 135 (9), 3070–3085, doi:10.1175/MWR3454.1.

690 Uhlhorn, E. W. and D. S. Nolan, 2012: Observational undersampling in tropical cyclones and  
691 implications for estimated intensity. *Mon. Wea. Rev.*, 140 (3), 825–840,  
692 doi:10.1175/MWR-D-11-00073.1.

693 Willoughby, H. E., E. N. Rappaport, and F. D. Marks, 2007: Hurricane forecasting: The state of  
694 the art. *Natural Hazards Review*, 8 (8), doi:10.1061/(ASCE)1527-6988(2007)8:3(45).

695

696 Tables and Figure Captions:

697

698 TABLE 1. List of Experiments.

699

700 Figure 1. Geometry of bistatic radar measurement of GPS-based quasi-specular surface  
701 scattering. The GPS direct signal (Transmitter) provides location, timing, and frequency  
702 references, while the forward scattered signal received by CYGNSS (Receiver) contains  
703 ocean surface information. Image from Claziria and Zavorotny (2015).

704

705 Figure 2. Basic flow chart of the regional OSSE framework.

706

707 Figure 3. Example of sampling of the North Atlantic by the simulated CYGNSS constellation,  
708 +/- 3 hours around 1500 UTC August 3, 2005. The locations of simulated CYGNSS data in the  
709 6-hour window are plotted as colored dots. The blue and green dots show the locations of  
710 subsets of all observations within +/- 1.5 hours and +/- 0.5 hours, respectively, of 1500 UTC.

711 CYGNSS observation locations are overlaid on the hurricane nature run (HNR1), 27-km  
712 resolution (d01) 10-meter wind speed field, valid at the same time.

713

714 Figure 4. Configuration of model domains. The 27-km resolution domain (d01) of HNR1 is  
715 shown in blue color, and the 9 km (d01) and nested 3 km (d02) OSSE grids are shown in a  
716 black color.

717

718 Figure 5. Average storm forecast errors with light +/- standard deviation lines plotted for 6-  
719 hourly (a, d, g), 3-hourly (b, e, h), and hourly (c, f, i) DA cycling experiments. Mean  
720 errors/deviations are colored by OSSE experiment: black/grey for CNTL, red/light red for  
721 CYG, and blue/light blue for VAM.

722

723 Figure 6. (a) Minimum sea-level pressure forecast error and (b) maximum wind speed  
724 forecast error of experiments CNTL3 (heavy dashed black) and CNTL1 (solid black) with  
725 respect to CNTL6 forecast errors. 95th percentile confidence intervals (CI) are plotted: 2-  
726 sided CIs are plotted in transparent gray and 1-sided CIs are plotted with a thin dash-dotted  
727 line for CNTL3 and a dotted line for CNTL1. (c) and (d) as in (a) and (b), but for CYG3 and  
728 CYG1 errors with respect to CYG6 forecast errors. (e) and (f) as in (a) and (b), but for VAM3  
729 and VAM 1 errors with respect to VAM6 forecast errors.

730

731 Figure 7. (a) Minimum sea-level pressure forecast error and (b) maximum wind speed  
732 forecast error of experiments CYG3 (red) and VAM3 (blue) with respect to CNTL3. 95<sup>th</sup>

733 percentile confidence intervals (CI) are plotted: 2-sided CIs are plotted in transparent colors  
734 and 1-sided CIs are plotted with thin dotted lines.

735

736 Figure 8. Large-scale, domain-averaged 10-meter wind errors (RMS,  $\text{m s}^{-1}$ ) for (a) 6-hourly  
737 DA cycling, (b) 3-hourly DA cycling and (c) hourly cycling. Experiments are plotted by color  
738 as in Fig. 5.

739

740 Figure 9. Absolute integrated kinetic energy (IKE) error (TJ) as a function of forecast hour for  
741 (a) 6-hourly DA cycling, (b) 3-hourly DA cycling and (c) hourly cycling. Error is the difference  
742 between OSSE experiment IKE and Nature Run IKE (HNR1).

743

744 Figure 10. (a) Nature Run 10-meter wind speed valid at 1800 UTC August 4 and (b-d) 24-  
745 hour forecasts of 10-meter wind speed from OSSE experiments CNTL3, CYG3 and VAM3,  
746 valid at the same time as (a). The instantaneous wind maximum ( $V_{\max}$ ) is labeled in the  
747 lower left in each panel.

748

749 Figure 11. As in Fig. 10 but for (a) Nature Run valid time of 1800 UTC August 5 and (b-d) 24-  
750 hour OSSE experiment forecasts valid at 1800 UTC August 5.

751

752

## Tables and Figures

TABLE 1. List of Experiments.

Experiment name	Description	Average Number of Observations Assimilated		
		6 hours	3 hours	1 hour
CTRL6, CTRL3, CTRL1*	Conventional Satellite/ Surface /sounding data; no CYGNSS.	51,547	25,773	8,591
CYG6, CYG3, CYG1*	CTRL plus all available CYGNSS wind speed (CYGNSS counts only)	15,091	7,545	2,517
VAM6, VAM3, VAM1*	CTRL plus VAM wind vectors at CYGNSS retrieval coordinates (CYGNSS counts only)	30,182	15,090	5,034

\* 6, 3 and 1 denote the cycle interval in h.

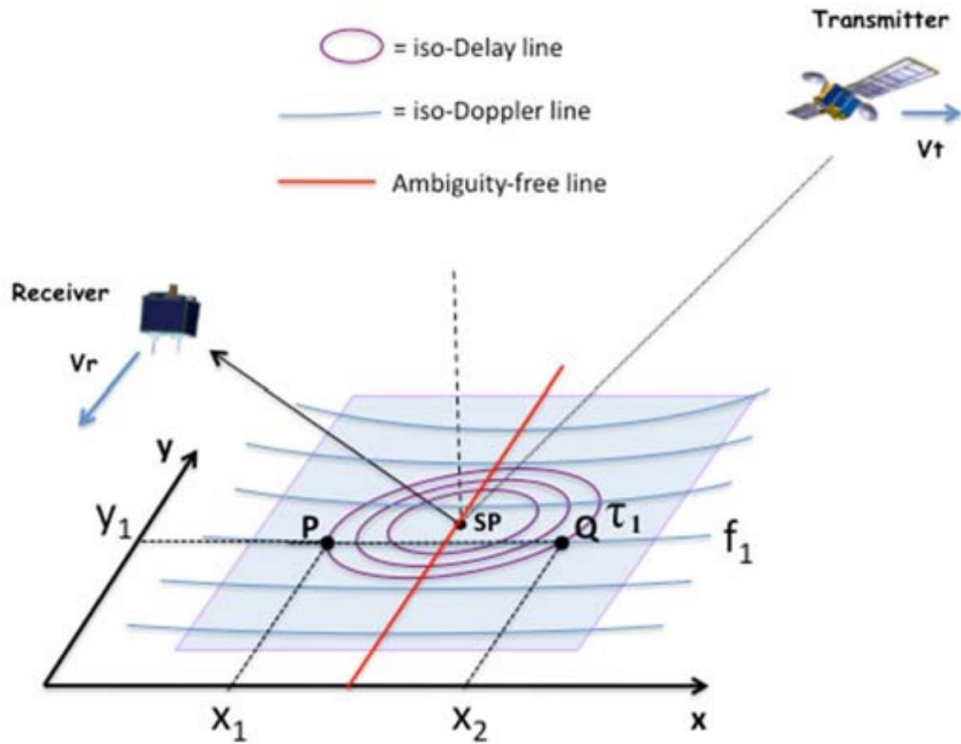


Figure 1. Geometry of bistatic radar measurement of GPS-based quasi-specular surface scattering. The GPS direct signal (Transmitter) provides location, timing, and frequency references, while the forward scattered signal received by CYGNSS (Receiver) contains ocean surface information. Image from Claziria and Zavorotny (2015).

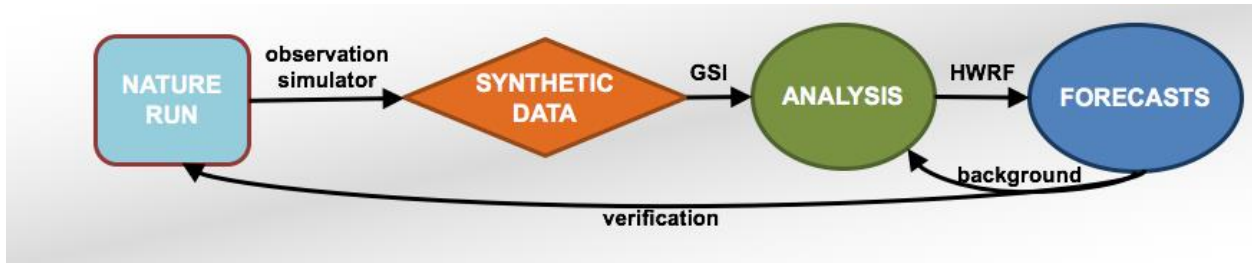


Figure 2. Basic flow chart of the regional OSSE framework.

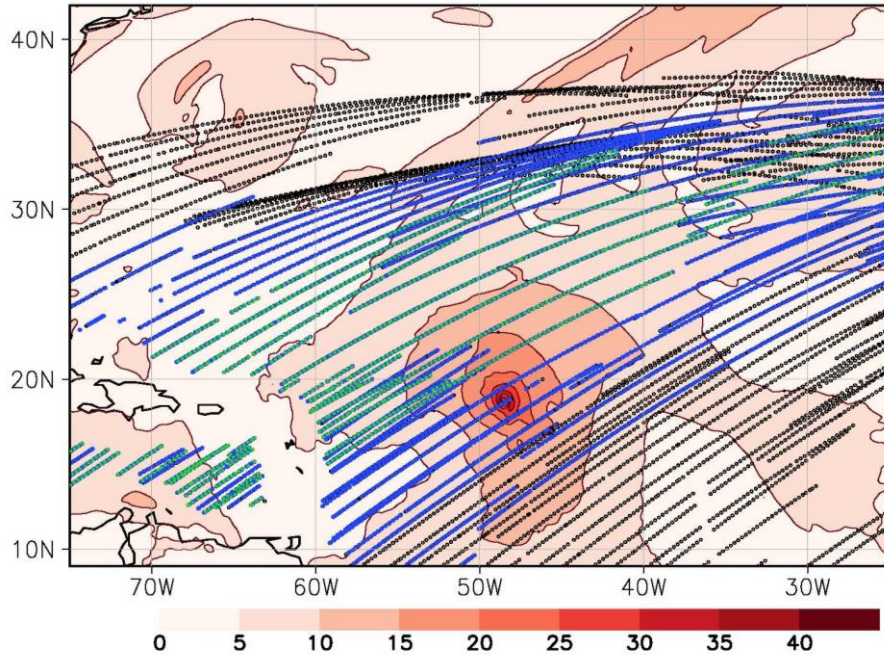


Figure 3. Example of sampling of the North Atlantic by the simulated CYGNSS constellation, +/- 3 hours around 1500 UTC August 3, 2005. The locations of simulated CYGNSS data in the 6-hour window are plotted as colored dots. The blue and green dots show the locations of subsets of all observations within +/- 1.5 hours and +/- 0.5 hours, respectively, of 1500 UTC. CYGNSS observation locations are overlaid on the hurricane nature run (HNR1), 27-km resolution (d01) 10-meter wind speed field, valid at the same time.

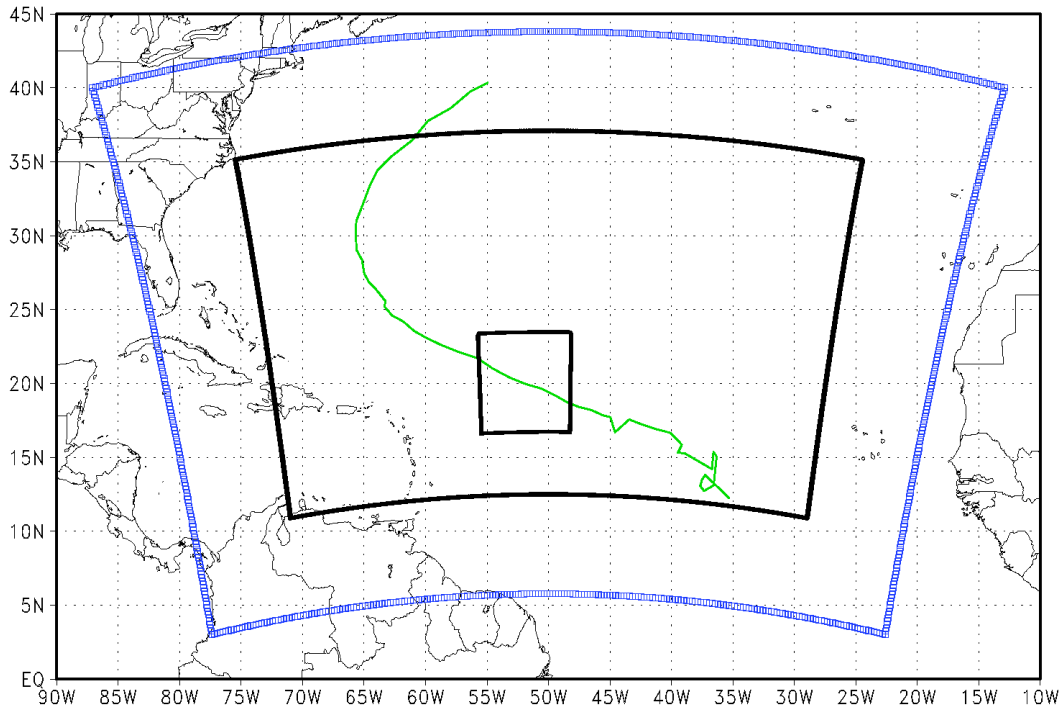


Figure 4. Configuration of model domains. The 27-km resolution domain (d01) of HNR1 is shown in blue color, and the 9 km (d01) and nested 3 km (d02) OSSE grids are shown in a black color.

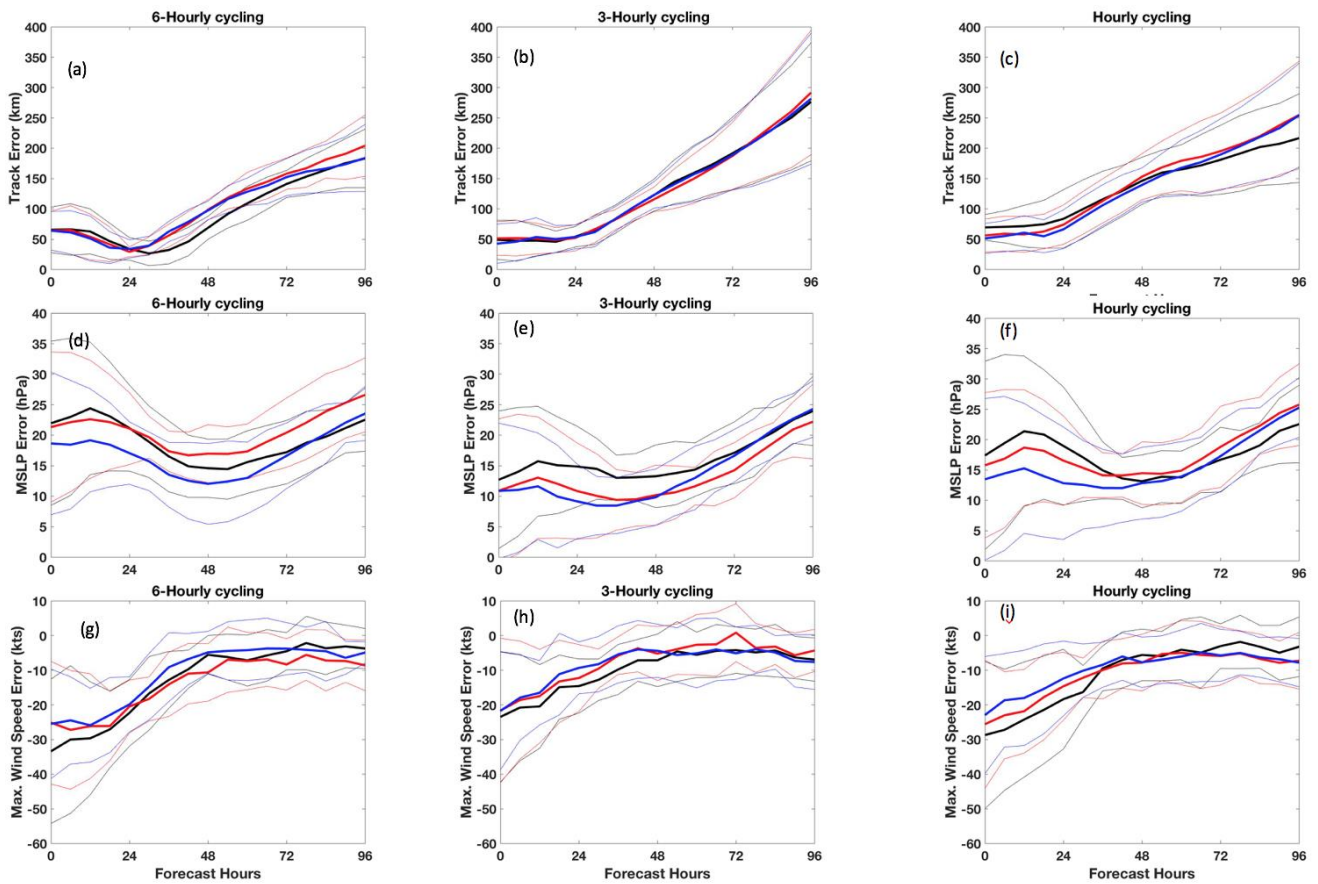


Figure 5. Average storm forecast errors with light +/- standard deviation lines plotted for 6-hourly (a, d, g), 3-hourly (b, e, h), and hourly (c, f, i) DA cycling experiments. Mean errors/deviations are colored by OSSE experiment: black/grey for CNTL, red/light red for CYG, and blue/light blue for VAM.

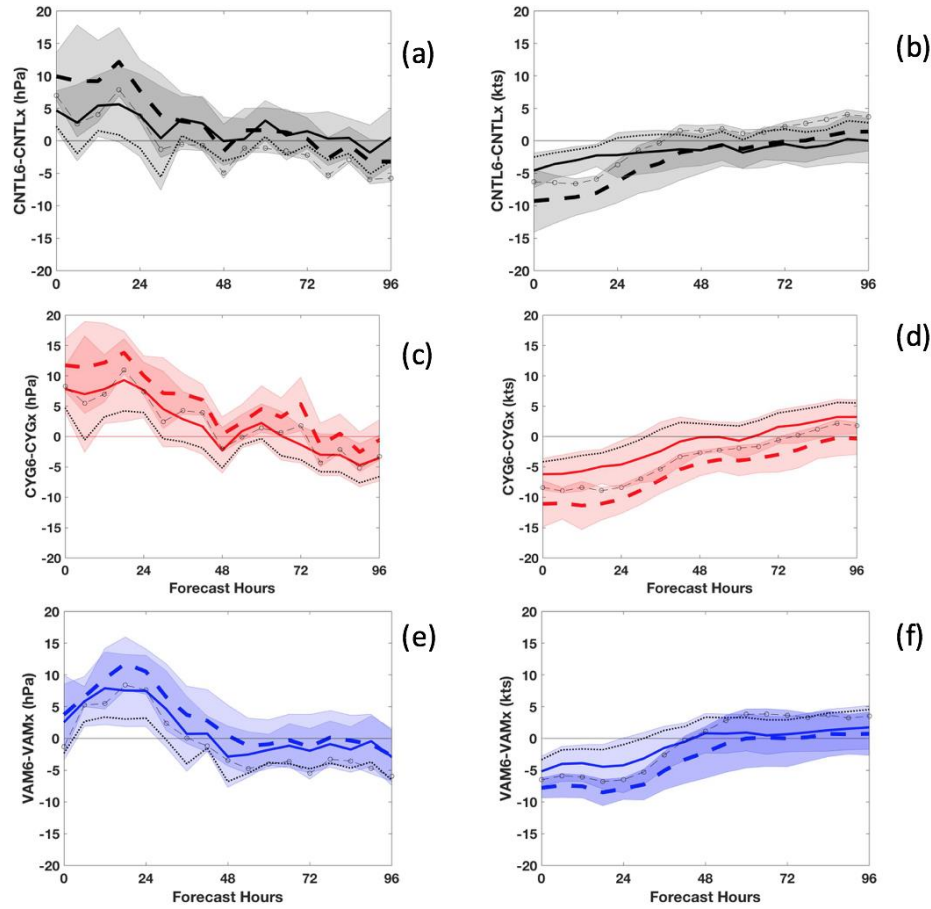


Figure 6. (a) Minimum sea-level pressure forecast error and (b) maximum wind speed forecast error of experiments CNTL3 (heavy dashed black) and CNTL1 (solid black) with respect to CNTL6 forecast errors. 95th percentile confidence intervals (CI) are plotted: 2-sided CIs are plotted in transparent gray and 1-sided CIs are plotted with a thin dash-dotted line for CNTL3 and a dotted line for CNTL1. (c) and (d) as in (a) and (b), but for CYG3 and CYG1 errors with respect to CYG6 forecast errors. (e) and (f) as in (a) and (b), but for VAM3 and VAM 1 errors with respect to VAM6 forecast errors.

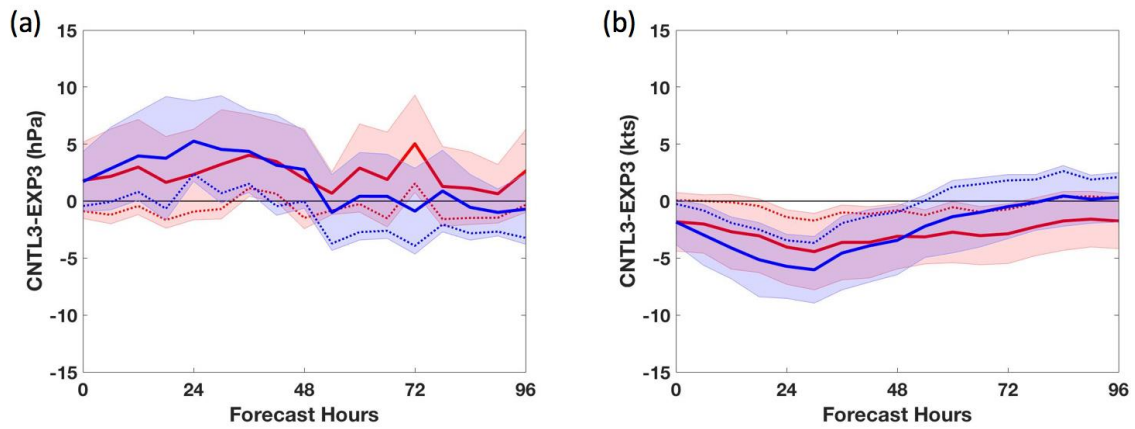


Figure 7. (a) Minimum sea-level pressure forecast error and (b) maximum wind speed forecast error of experiments CYG3 (red) and VAM3 (blue) with respect to CNTL3. 95th percentile confidence intervals (CI) are plotted: 2-sided CIs are plotted in transparent colors and 1-sided CIs are plotted with thin dotted lines.

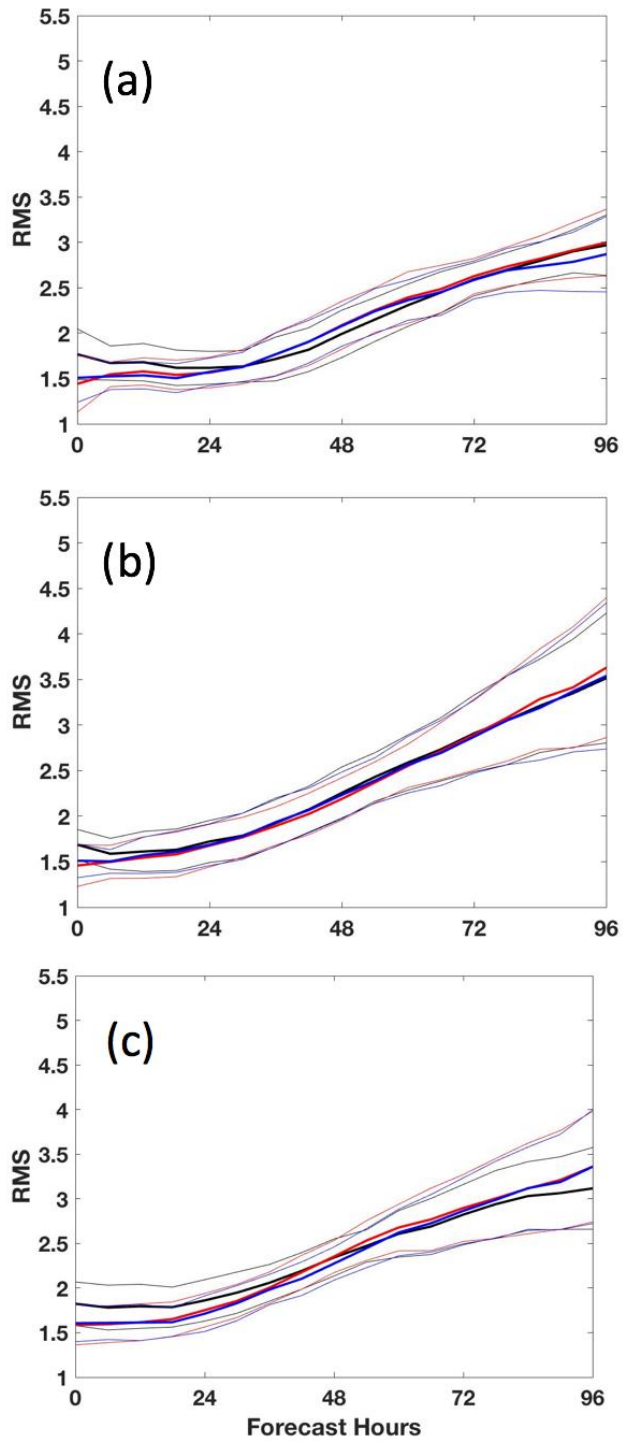


Figure 8. Large-scale, domain-averaged 10-meter wind errors (RMS, m s<sup>-1</sup>) for (a) 6-hourly DA cycling, (b) 3-hourly DA cycling and (c) hourly cycling. Experiments are plotted by color as in Fig. 5.

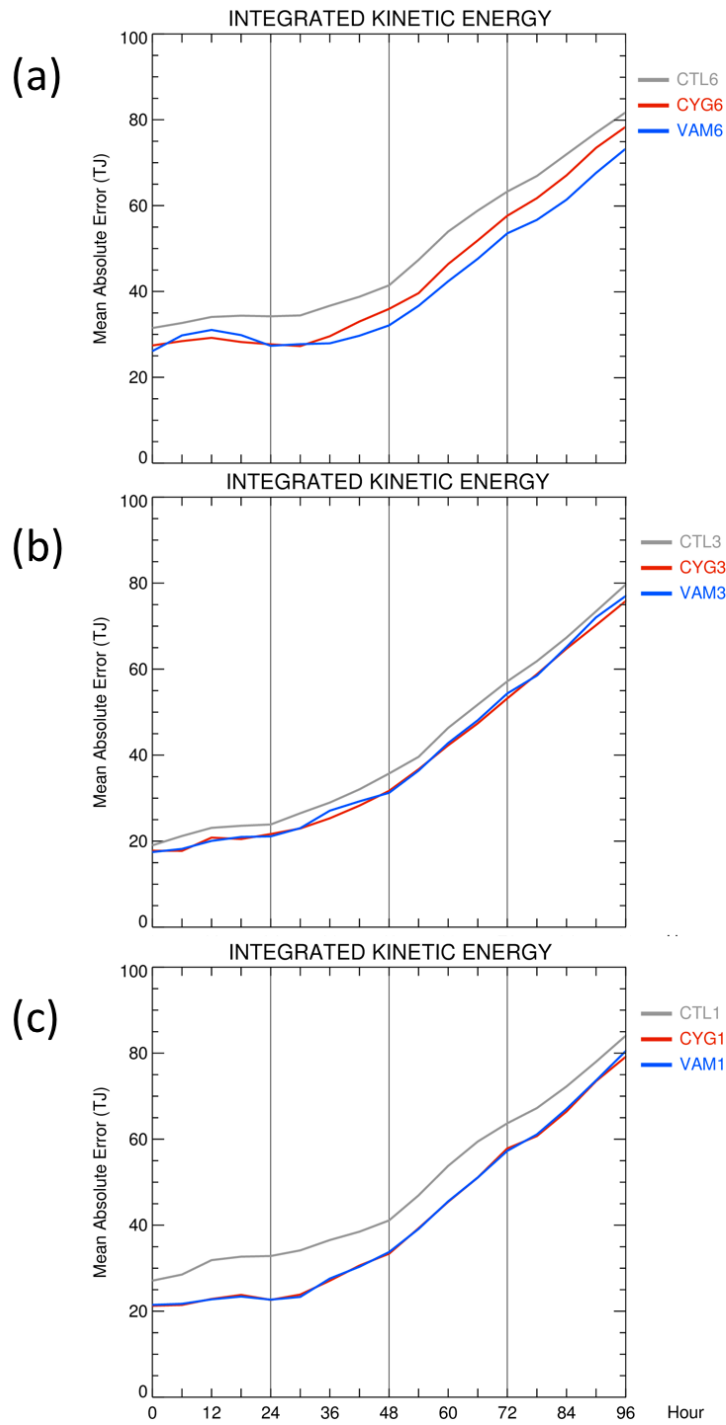


Figure 9. Absolute integrated kinetic energy (IKE) error (TJ) as a function of forecast hour for (a) 6-hourly DA cycling, (b) 3-hourly DA cycling and (c) hourly cycling. Error is the difference between OSSE experiment IKE and Nature Run IKE (HNR1).

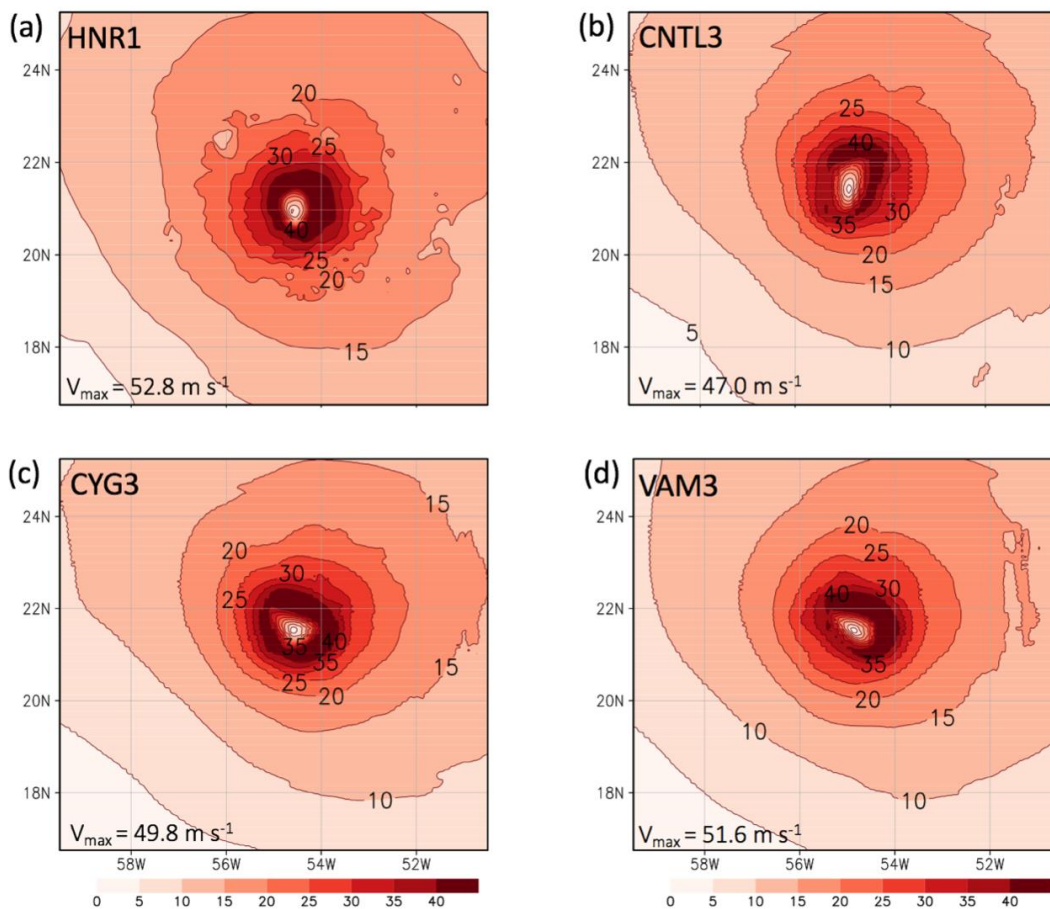


Figure 10. (a) Nature Run 10-meter wind speed valid at 1800 UTC August 4 and (b-d) 24-hour forecasts of 10-meter wind speed from OSSE experiments CNTL3, CYG3 and VAM3, valid at the same time as (a). The instantaneous wind maximum ( $V_{\text{max}}$ ) is labeled in the lower left in each panel.

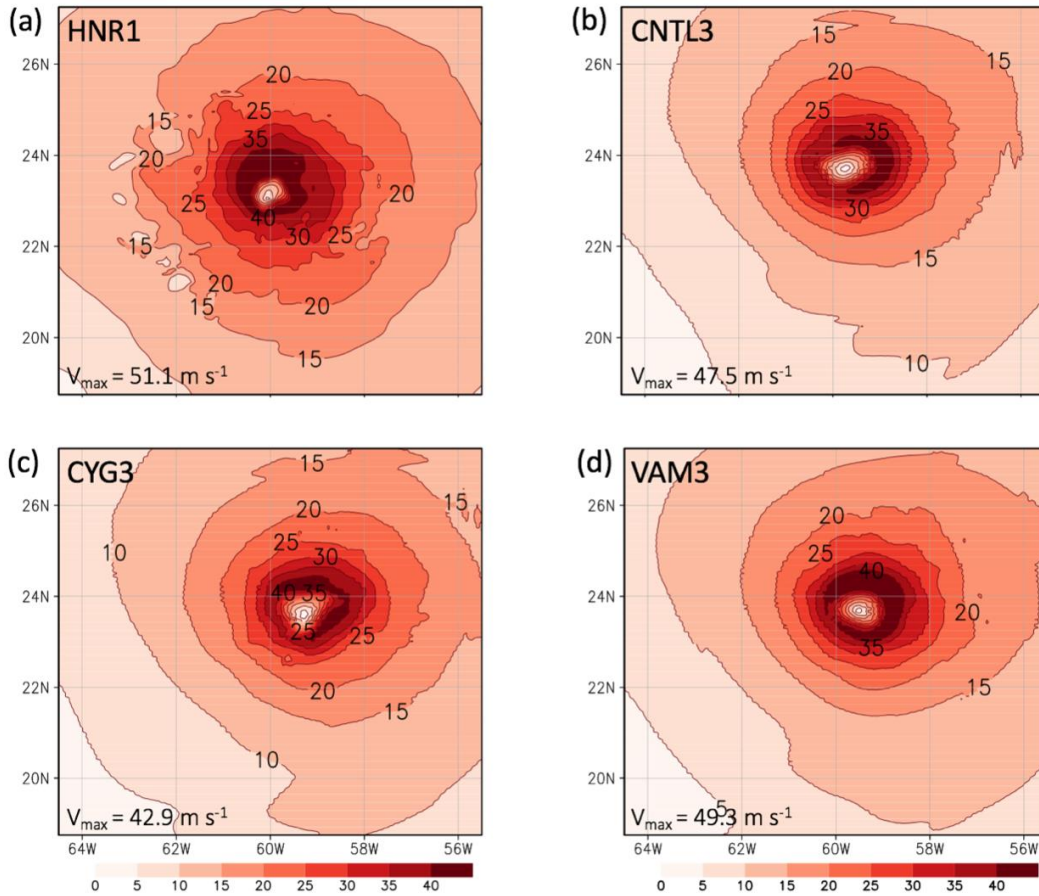


Figure 11. As in Fig. 10 but for (a) Nature Run valid time of 1800 UTC August 5 and (b-d) 24-hour OSSE experiment forecasts valid at 1800 UTC August 5.